

# Chapter 7. Dynamics of field-induced droplet ionization. Time resolved studies of distortion, jetting, and progeny formation from charged and neutral methanol droplets exposed to strong electric fields

Adapted from Grimm, R.L. and Beauchamp, J.L. *J. Phys. Chem. B.* **2005**, *109*, 8244.

## 7.1. Abstract

We recently reported that strong electric fields may be employed to directly extract positive and negative ions for mass analysis, including intact proteins, from neutral droplets. The present study investigates the dynamics of this process using switched high electric fields to enable time-resolved studies of droplet distortion, Taylor cone formation, and charged progeny droplet extraction from neutral and charged 225 micron methanol droplets. After a specific time in the field, a flashlamp is triggered to record droplet distortions using shadow photography. At a critical field strength  $E_c^0$  corresponding to the Taylor limit, neutral droplets exhibit a prolate elongation along the field axis forming symmetric cone-jets of positive and negatively charged progeny droplets, approximately 10 microns in diameter. This process is termed field-induced droplet ionization (FIDI). Because the timescale of FIDI is related to the frequency of shape oscillations that occur below the Taylor limit, models of field-dependent oscillation become an important predictor of the timescale for progeny jet formation. Droplets with a net charge  $q$  distort into asymmetric tear shapes and emit a single charged jet of

progeny at a critical field  $E_c^q$  that is less than  $E_c^0$ . The measured decrease in droplet stream charge indicates that total charge loss can be greater than the original charge on the droplet, resulting in oppositely charged droplets. Interestingly, above  $E_c^0$ , charged droplets sequentially emit a jet of the same polarity as the net charge followed by a jet of reverse polarity emitted in the opposite direction. For both neutral and charged droplets, increasing the electric field decreases the time to form jets and the combination of net charge and higher-than-critical fields has a compound effect in accelerating progeny formation. The implications of our results for using switched fields in FIDI-mass spectrometry for on-demand ion sampling from neutral and charged droplets are discussed.

## 7.2. Introduction

Recent advances in understanding the effect of high electric fields on droplets have created new analytical methodologies for extracting and mass analyzing biomolecules from solution. In a sufficiently strong electric field, droplets elongate parallel to the field and develop two opposing Taylor cones that emit oppositely charged jets of small progeny droplets. When an analyte is dissolved in the droplets, the jets are a viable source of gas-phase analyte ions for mass spectrometry.<sup>1</sup> Termed field-induced droplet ionization (FIDI), the practical application of this experimental methodology will rely on detailed investigations of the dynamics of the process and a more complete understanding of the parameter space associated with the phenomenon. For example, given the specific size, composition, and charge of an individual droplet, mass spectrometric sampling by FIDI requires knowledge of the magnitude of the electric field

required to produce jetting, the timescale of the event, and the efficiency with which analyte species are converted into the gas-phase ions and sampled by a mass spectrometer.

Droplet response to both electric fields and excess charge has been investigated for over a century. Although early motivations focused on the effect of electric fields on droplets within clouds,<sup>2-4</sup> more recent research has considered a broad range of applications from the technologically important processes of electrostatic spraying<sup>5</sup> to the revolution in mass spectrometric studies of biological molecules made possible by electrospray ionization.<sup>6-11</sup> Lord Rayleigh first considered the electrical pressure resulting from excess charge  $q$  on a droplet of spherical radius  $r$  and surface tension  $\sigma$ . He surmised that the natural quadrupolar oscillation of a droplet in a field-free environment becomes unstable when  $q$  exceeds the limit  $q_R$ , now known as the Rayleigh limit, defined in equation (7.1).

$$q_R = 8\pi(\sigma\epsilon_0 r^3)^{1/2} \quad (7.1)$$

Equation (7.1) and all later equations are reported in MKS units and  $\epsilon_0$  is the permittivity of free space. Non-dimensional electric fields used in the literature<sup>12,13</sup> are dimensionalized as appropriate by the characteristic field strength  $(2\sigma/\epsilon_0 r)^{1/2}$  and non-dimensional frequencies are divided by the characteristic time  $(\rho r^3/\sigma)^{1/2}$  where  $\rho$  is the droplet density. At  $q \geq q_R$ , a limit reached when a charged droplet evaporates to a sufficiently small size, Rayleigh postulated that the droplet would throw out liquid in fine jets<sup>14</sup> in an event alternatively referred to as Rayleigh discharge<sup>10,11</sup> or Coulomb fission.<sup>9</sup> The Rayleigh limit has been researched extensively and is widely used to explain the behavior of highly charged droplets formed by electrospray ionization.<sup>9,15,16</sup>

The FIDI process results from the distortion and jetting of droplets subjected to a high electric field. Early experimental<sup>3,4,17,18</sup> and theoretical<sup>19,20</sup> work showed that neutral droplets symmetrically elongate parallel to the electric field as polarization-induced charge densities develop at opposite ends of the prolate spheroid. This shape becomes unstable when the applied electric field reaches a critical limit,  $E_c^0$ , given by (7.2). This

$$E_c^0 = \frac{c}{(8\pi)^{1/2}} \left( \frac{2\sigma}{\epsilon_0 r} \right)^{1/2} \quad (7.2)$$

critical field is known as the Taylor limit named for G. I. Taylor who pioneered the corresponding theory. In equation (7.2), the fitting constant  $c$  has been determined both empirically<sup>3,4,18,21</sup> and theoretically,<sup>20</sup> and the accepted value is 1.625 for liquid droplets in air.<sup>20</sup> Assuming droplets always distort into spheroidal shapes, Taylor additionally derived (7.3) and (7.4), the general relationship between an applied electric field  $E < E_c^0$

$$E = I_2 \gamma^{-4/3} \left( 2 - \gamma^{-3} - \gamma^{-1} \right)^{1/2} \left( \frac{2\sigma}{\epsilon_0 r} \right)^{1/2} \quad (7.3)$$

and the resulting aspect ratio  $\gamma = a / b$  of the major to minor axis of the spheroid.<sup>20</sup> In equation (7.3), the coefficient  $I_2$  is a higher-order function of  $\gamma$  represented by (7.4).

$$I_2 = \frac{1}{2(1-\gamma^{-2})^{3/2}} \ln \left[ \frac{1 + (1-\gamma^{-2})^{1/2}}{1 - (1-\gamma^{-2})^{1/2}} \right] - \frac{1}{1-\gamma^{-2}} \quad (7.4)$$

Although a simple relation does not exist for  $\gamma(E)$  in the spheroidal approximation, equation (7.5) approximates the relationship between  $\gamma$  and  $E$  in (7.3) to within 1% for

$$\gamma(E) = \left( 1 + \frac{9r\epsilon_0 E^2}{16\sigma} \right) \left( 1 - \frac{9r\epsilon_0 E^2}{16\sigma} \right)^{-1} \quad (7.5)$$

fields less than 55% of the Taylor limit.<sup>22</sup> Equation (7.3) predicts  $\gamma$  increases with increasing  $E$  until  $\gamma = 1.85$  where the droplet becomes unstable corresponding to  $E = E_c^0$ . This relationship is supported by experimental and theoretical evidence for neutral droplets and soap films in air.<sup>3,12</sup>

Between the Rayleigh limit of charge and the Taylor limit of field exists the general case where excess electrical pressure within a droplet results from both net charge and the externally applied electric field. Taylor's spheroidal approximation is not as accurate at predicting shapes and critical fields because charged droplets are shown to be egg- or tear-shaped,<sup>12,23,24</sup> having a higher curvature on the side carrying the net charge. For a droplet of charge  $q$ , this shape becomes unstable at a critical electric field,  $E_c^q$ , and is characterized by the formation of a single jet from the sharper end. The critical field is a function of net charge as increasing charge reduces the field necessary to create an instability, or  $0 \leq E_c^q \leq E_c^0$  for  $0 \leq q \leq q_R$ . Recent investigations of jetting, fissioning, and Taylor cones focus on droplets suspended in an ambient liquid.<sup>25-27</sup> This work bears little application to FIDI, which is performed in an ambient gas so that the progeny jets may be directed towards the inlet of an atmospheric-sampling mass spectrometer.

In the present investigation, we characterize the temporal evolution of droplet shapes leading to FIDI events as a function of electric field strength and droplet net charge following exposure of the droplet to a rapidly switched electric field. A vibrating orifice aerosol generator (VOAG)<sup>28</sup> generates a monodisperse stream of 225  $\mu\text{m}$  methanol droplets whose Taylor limit from (7.2) is  $2.16 \times 10^6 \text{ V/m}$ , somewhat close to the breakdown limit of air.

This work partitions the study of droplets into three specific cases. The first case considers the time-dependent shape oscillations of neutral droplets at fields below  $E_c^0$ . The oscillation frequency is field-dependent and is a useful predictor for the timescale for FIDI as  $E$  approaches  $E_c^0$ . Fitted experimental  $\gamma(t)$  values are compared to literature models discussed in the experimental section.

The second case considers neutral droplets in fields at and above  $E_c^0$ . FIDI events are characterized by the highly elliptical shape and presence of jetting from conical tips as a function of time and strength of the applied electric field. Field strengths required for FIDI are compared to eq (7.2) and the timescale for jetting to occur is related to droplet oscillation frequencies from the first case.

The third case investigates droplets between 4% and 13% of their Rayleigh limit of charge in fields at and above their critical field,  $E_c^q$ . The decrease in  $E_c^q$  as a function of  $q$  is explored and related to models developed by Basaran and Scriven<sup>12</sup> and by Abbas and Latham.<sup>24</sup>

### **7.3. Experimental section**

#### **7.3.1. Droplet production and charging**

Figure 7.1 shows a schematic of the experimental apparatus. A vibrating orifice aerosol generator (VOAG) creates a monodisperse droplet stream. HPLC-grade methanol (EMD Chemicals Inc.) is used without further purification. A nitrogen-backed solution reservoir (not shown) delivers methanol to the VOAG. Nitrogen gas (1 - 3 psig) pumps the methanol giving a smoother flow rate and a more stable stream than a syringe pump. A 130  $\mu\text{m}$  I.D. ceramic orifice (4P480-0016-343; Kulicke and Soffa Inc., Willow

Grove, PA, USA) is mounted within an annular piezoelectric actuator vibrating in the direction of the methanol flow at 11.4 kHz. The  $\sim 5 \text{ m s}^{-1}$  stream breaks into droplets that pass through a grounded aperture.

Droplet charge is governed by the local electric field at the point at which the stream breaks into droplets. Before the orifice, the methanol passes through a metal charging ring connected to a voltage supply,  $V_C$ , establishing a field between the stream and the grounded aperture. Setting  $V_C$  to ground generates neutral droplets while increasing  $V_C$  between 0 and 600 V linearly increases the net charge between 0% and 13% of the Rayleigh limit. Higher net charge results in excessive space-charge repulsion between the droplets causing a disruption of the stream. A digital picoammeter (model 485, Keithley Instruments, Inc.) measures the total current to ground resulting from the droplets impacting a metal collector. Individual droplet charge is calculated from this current and the droplet production rate. A step-function drop in the picoammeter current indicates the amount of charge droplets lose during FIDI by comparing the current from droplets both before and after FIDI events. Droplet charging is not affected by other electric fields in the experiment.

### 7.3.2. Pulsed field experiment

The droplets pass between two 6.5 mm long parallel-plate electrodes spaced 1.4 mm apart that define the FIDI region. Calculations in SIMION<sup>29</sup> verify the field gradient approximates a parallel-plate capacitor to within 4% over 88% of its length when the droplet path bisects the electrodes. In our earlier experiments, this field was

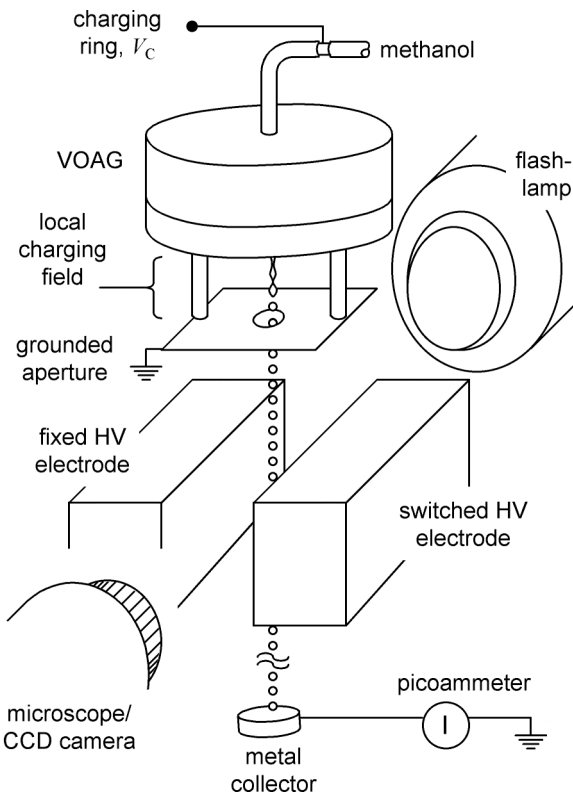


Figure 7.1. Schematic diagram of the experiment. Methanol is delivered to a vibrating orifice aerosol generator (VOAG) that breaks a liquid stream into monodisperse  $225\text{ }\mu\text{m}$  droplets at  $11.4\text{ kHz}$ . A voltage applied to the stream by a charging ring held at  $V_C$  relative to the grounded aperture determines droplet net charge. Droplets pass between the parallel electrodes that define the high-field region. The left electrode is held at a fixed high voltage (HV) while the opposing electrode is switched from HV to ground. After exposure to the high field for a time  $t$ , a flashlamp behind the stream illuminates the droplets and a microscope fitted with a CCD camera records the resulting shadowgraph. A metal collector intercepts the droplet stream and a picoammeter quantifies droplet charge.

fixed by holding one electrode at high voltage (HV) and the other at ground, resulting in a gradual increase in the field experienced by droplets as they entered the high-field region.<sup>1</sup> In the present experiment, droplets enter this region when both electrodes are held at an identical high voltage between 2.8 and 3.4 kV creating a field-free region. The left electrode maintains a fixed HV while a stacked circuit of MTP1N100E MOSFETs switches the right-hand plate from HV to ground and remains there for a variable time  $t = 10 - 900 \mu\text{s}$  before returning to high-voltage. As a result, droplets are in a well-defined electric field until they are photographed. Based on similar circuits from the literature,<sup>30,31</sup> this in-house design is capable of switching up to 4 kV to ground in less than 1  $\mu\text{s}$ . Rather than using an avalanche transistor<sup>30</sup> or a transmission line<sup>31</sup> to drive the FETs, a 6N135 optoisolator drives each FET and isolates the remainder of the electronics from a possible surge or breakdown.

After the variable time,  $t$ , following exposure to the high field, a sub-microsecond xenon flashlamp illuminates the droplets. The flashlamp is mounted behind the FIDI region and directs a collimated beam directly at a microscope focused on the droplets. Using a 10x objective, a 10x wide-angle eyepiece adapter (MaxView Plus, Scopetronix, Cape Coral, FL, USA) and an afocally-coupled CCD camera (C-5060 wide zoom, Olympus), the optical train resolves 5  $\mu\text{m}$  features. Acquiring images of droplets and progeny for  $t$  ranging from 10 to 900  $\mu\text{s}$  generates a time-history of droplet response to a specific high electric field.

### 7.3.3. Determining the aspect ratio and model comparison

Each shadowgraph contains 3-5 droplets. For each droplet image, a custom LabView-based edge analysis program developed by the Leisner research group<sup>32</sup> fits an ellipsoid that provides aspect ratio and size information. The program verifies the monodispersity of the droplets and computes aspect ratios of 10-20 droplets for each  $t$  and electric field strength. The time-dependent aspect ratio,  $\gamma(t)$  is fitted to a damped sine function (7.6). In eq (7.6),  $v$  is the fitted oscillation frequency in  $s^{-1}$ ,  $A$  is the amplitude,  $\phi$  is the phase,  $\gamma_\infty$  is the equilibrium aspect ratio or  $\gamma(t=\infty)$ , and  $g$  is the exponential dampening constant. Oscillation frequencies are compared to numerical solutions by Basaran and co-workers<sup>13</sup> and to analytical solutions by Feng and Beard<sup>33</sup> and by Brazier-Smith and co-workers.<sup>34</sup> Feng and Beard found the field-dependent oscillation frequency  $v^{\text{FB}}$  to be eq (7.7). They suggest the frequency decreases proportionally with  $E^2$  until reaching  $E_c^0$  where the frequency is given by eq (7.8). Brazier-Smith and co-workers derived the oscillation,  $v^{\text{BS}}$ , as a function of the equilibrium aspect ratio, (7.9).

$$\gamma(t) = \gamma_\infty + A \sin(2\pi vt + \phi) \exp(-gt) \quad (7.6)$$

$$v^{\text{FB}} = \frac{8^{1/2}}{2\pi} \left[ 1 - 2.764 E^2 \left( \frac{\epsilon_0 r}{2\sigma} \right) \right] \left( \frac{\sigma}{r^3 \rho} \right)^{1/2} \quad (7.7)$$

$$v^{\text{FB}}(E_c^0) = \frac{8^{1/2}}{2\pi} \left[ 1 - 2.764 \frac{1.625^2}{8\pi} \right] \left( \frac{\sigma}{r^3 \rho} \right)^{1/2} \quad (7.8)$$

$$v^{\text{BS}} = \frac{8^{1/2}}{2\pi} x^{1/2} \left( \frac{\sigma}{r^3 \rho} \right)^{1/2} \quad (7.9)$$

In eq (7.9),  $x$  is a multi-component function of  $\gamma$ . Combining the relationships between  $\gamma$  and  $v^{BS}$  in eq (7.9) and  $\gamma$  and  $E$  in eq (7.3), Brazier-Smith and co-workers predict  $v^{BS}$  decreases to 0 as  $E$  approaches  $E_c^0$ .<sup>34</sup> Equations (7.7) and (7.9) reduce to the natural  $l = 2$  mode shape oscillation at  $E = 0$ .

The LabView program determines the aspect ratio assuming a spheroidal shape, which limits rigorous analysis to neutral droplets. Since charged droplets in electric fields are tear-shaped, analysis of the aspect ratio is limited to qualitative comparisons. While this study explores neutral droplets below  $E_c^0$ , we do not consider charged droplets below  $E_c^q$ .

## 7.4. Results and discussion

### 7.4.1. Case One. Neutral droplets below the critical field

Droplets in fields below  $E_c^0$  undergo damped oscillation. Figure 7.2 highlights a sequence of droplets in a  $2.00 \times 10^6$  V/m electric field. Initially,  $\gamma(0 \mu\text{s}) = 1$  corresponding to the spherical droplet (A). A damped shape oscillation is marked by increasing aspect ratios in (B)-(E), decreasing aspect ratios in (E)-(I), and increasing again in (J). Figure 7.3 highlights this trend in plots of  $\gamma$  versus the time in the electric field for four field strengths below  $E_c^0$ . Each point represents the average aspect ratio for approximately ten images at each respective time, and is fit to the exponentially damped sine function (7.6). The fitted equilibrium aspect ratios,  $\gamma_\infty$ , strictly increase as the electric field increases and are in excellent agreement with Taylor's theoretical model, (7.3), for each respective electric field.

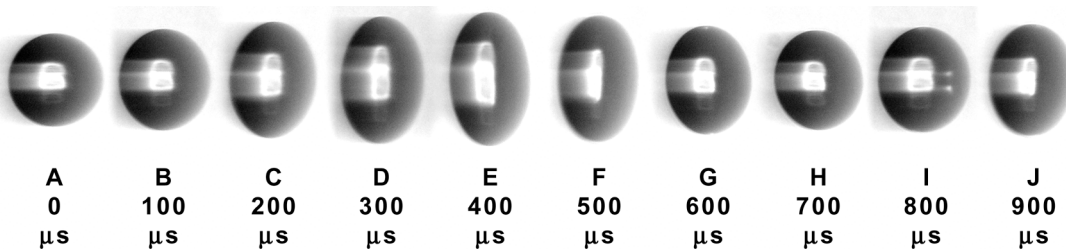


Figure 7.2. Neutral 225  $\mu\text{m}$  diameter methanol droplets are exposed to a  $2.00 \times 10^6 \text{ V/m}$  electric field for the indicated time period. Initially, droplets are spherical (A). Through 400  $\mu\text{s}$ , droplets distort into prolate ellipsoids with increasing aspect ratios. Between 400 (E) and 800  $\mu\text{s}$  (I), the aspect ratios decrease, only to increase again beginning at 900  $\mu\text{s}$  (J). This shape oscillation is characteristic of neutral droplets in fields below their Taylor limit.

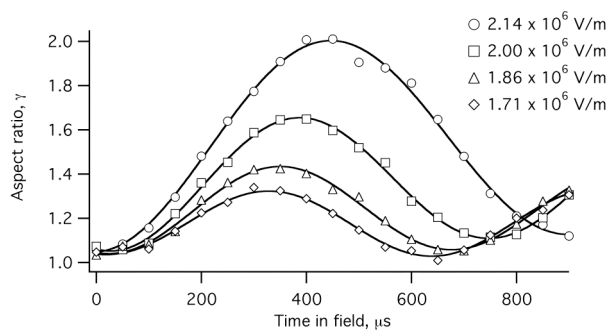


Figure 7.3. Average aspect ratio,  $\gamma$ , versus time for 225  $\mu\text{m}$  diameter methanol droplets in fields below  $E_c^0$  where the spheroid shape oscillates until reaching equilibrium. This shape is characterized by  $\gamma$ , the ratio of the major to minor axis of the spheroid. As the applied electric field increases, the amplitude of the oscillation increases and the frequency decreases in qualitative agreement with theoretical models.

Figure 7.4 compares the fitted oscillation frequencies from this work (round markers) with the Feng and Beard frequency  $\nu^{\text{FB}}$  (solid line), the Brazier-Smith and co-workers frequency  $\nu^{\text{BS}}$  (dashed line), and the numerical simulations of Basaran and co-workers (triangle markers, dotted line) which are each dimensionalized for 225 micron methanol droplets. Error bars represent how the uncertainty in the aspect ratio data is reflected in the oscillation frequency. For each electric field strength, uncertainty in the frequency is bounded by fitting the damped sine function to plots of the average aspect ratio minus the standard deviation and plus the standard deviation. The maximum error in the fitted frequency values is 7%. The fitted values from this work follow each of the theoretical trends with decreasing frequencies as the applied field increases. The initial values closely match  $\nu^{\text{FB}}$  but diverge to lower frequencies at higher field strengths.

#### 7.4.2. Case Two. Neutral droplets above the critical field

Figure 7.5 shows 225  $\mu\text{m}$  diameter droplets symmetrically elongating and jetting at two field strengths. Droplets oscillate at  $2.14 \times 10^6 \text{ V/m}$  as shown by Figure 7.3 and undergo FIDI in a  $2.18 \times 10^6 \text{ V/m}$  field, in good agreement with the value of  $E_c^0$  predicted by (7.2). In a  $2.18 \times 10^6 \text{ V/m}$  field, jetting begins after 650  $\mu\text{s}$  (Figure 7.5E), whereas jetting occurs as early as 350  $\mu\text{s}$  in a  $2.46 \times 10^6 \text{ V/m}$  field (Figure 7.5J). Thus, the 13% increase in the electric field above  $E_c^0$  accelerates the elongation and reduces the time to form jets by 46%. Figure 7.6 graphs  $\gamma(t)$  for fields between 2.18 and  $2.42 \times 10^6 \text{ V/m}$  as well as the fitted oscillation  $\gamma(t)$  at  $2.14 \times 10^6 \text{ V/m}$  reproduced from Figure 7.4. Figure 7.6 illustrates this reduction in time to achieve jetting which results

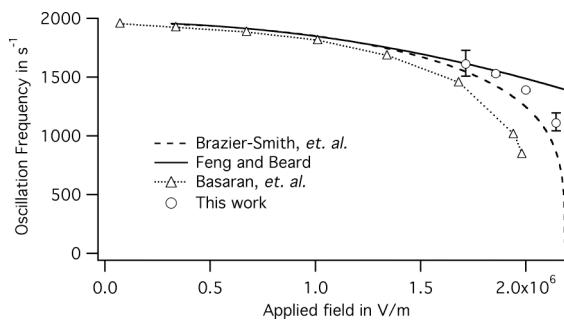


Figure 7.4. Comparison of fitted oscillation frequencies to predictions of Brazier-Smith and co-workers (dashed line), of Feng and Beard (solid line), and of Basaran and co-workers (triangle markers, dotted line) applied to 225  $\mu\text{m}$  methanol droplets. Error bars represent the frequency of damped sine fits to the average aspect ratio values plus and minus the respective standard deviations, respectively. Fitted values from this work (round markers) follow the theoretical trends in all models, most closely matching the predictions of Brazier-Smith and co-workers.

from increasing the applied field. For droplets at  $E_c^0$ , conical shapes begin to form at aspect ratios between 2.5 and 3 following exposure to the high field. At the onset of jetting, the aspect ratio is approximately 3.2. This is consistent over the range of electric fields employed indicating that only the time to reach jetting is affected by field strength, and the shape at the onset remains consistent.

Figure 7.6 highlights a fundamental relationship between the droplet oscillation in fields below  $E_c^0$ , and the elongation leading to FIDI in the critical field. Through 450  $\mu\text{s}$ , or half the oscillation period, the oscillation closely tracks the aspect ratio of droplets undergoing FIDI at  $E_c^0$ . Beyond 450  $\mu\text{s}$ , the aspect ratio of oscillating droplets decreases while the aspect ratio of droplets undergoing FIDI continues to increase. This pattern corroborates the non-dimensional calculations of Basaran and coworkers.<sup>13</sup> Therefore the response of a droplet in fields slightly below and at  $E_c^0$  are proportionally linked and the shape oscillation of a droplet near the critical field becomes an important predictor for the timescales for progeny jet formation at  $E_c^0$ . Equation (7.10) empirically relates both the 650  $\mu\text{s}$  time to initiate FIDI,  $\tau_{\text{FIDI}}$ , to the 900  $\mu\text{s}$  oscillation period,  $\nu^{-1}$ , for 225  $\mu\text{m}$  droplets and  $\tau_{\text{FIDI}} = 575 \mu\text{s}$  to  $\nu^{-1} = 800 \mu\text{s}$  for similar investigations on 200  $\mu\text{m}$  droplets.

$$\tau_{\text{FIDI}} \approx 0.75 \left( \nu_{E \rightarrow E_c^0} \right)^{-1} \quad (7.10)$$

Equation (7.10) is comparable to non-dimensional calculations that show a ratio of  $\sim 0.6$  between the timescale for a droplet to elongate to  $\gamma = 3.2$  in fields above  $E_c^0$  to the oscillation period slightly below  $E_c^0$ .<sup>13</sup>

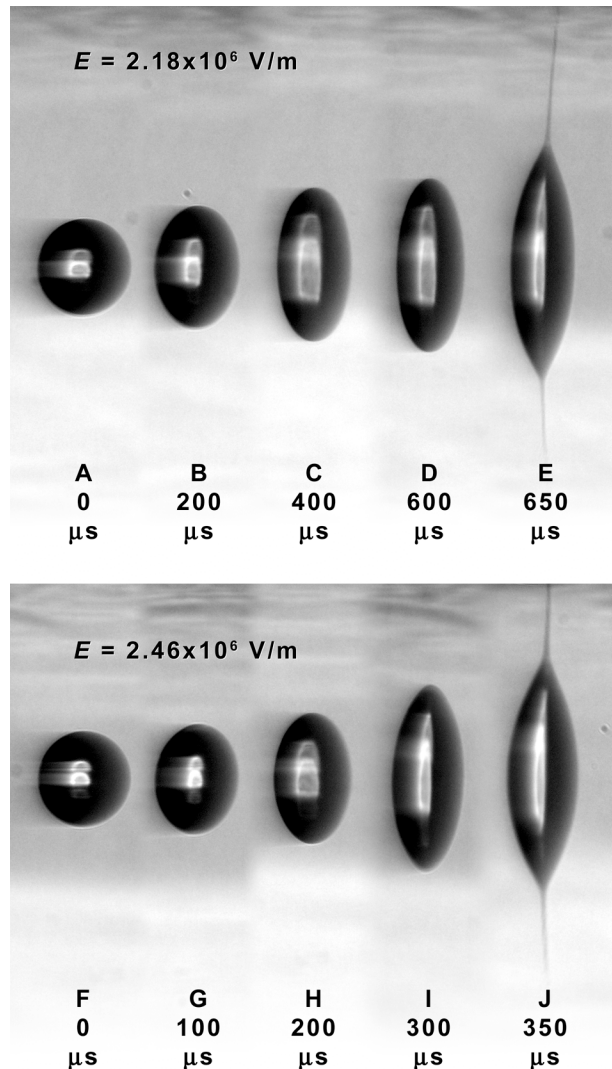


Figure 7.5. Sequences of 225  $\mu\text{m}$  droplets exposed to an electric field for the indicated time period. Frames (A)-(E) represent droplets in a  $2.18 \times 10^6 \text{ V/m}$  field while frames (F)-(J) demonstrate FIDI in a  $2.46 \times 10^6 \text{ V/m}$  field. Each sequence is characterized by symmetrical elongation as exposure to the field increases, culminating in the formation of two conical tips and oppositely charged progeny jets characteristic of FIDI. At  $2.18 \times 10^6 \text{ V/m}$ , FIDI develops after 650  $\mu\text{s}$  in (E) while the stronger field results in accelerated elongation and progeny formation after 350  $\mu\text{s}$  in (J).

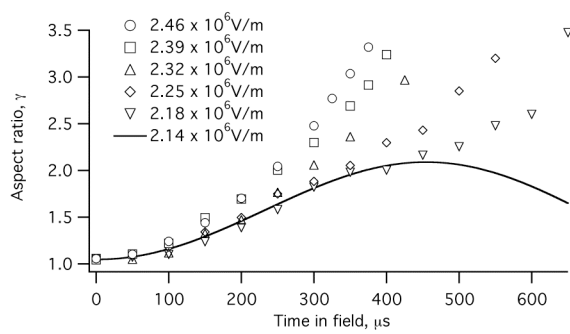


Figure 7.6. Average aspect ratio,  $\gamma$ , versus time for 225  $\mu\text{m}$  diameter methanol droplets in fields sufficiently high for FIDI. The oscillation fit from droplets in a  $2.14 \times 10^6 \text{ V/m}$  field is included for comparison. Because the droplets oscillate at  $2.14 \times 10^6 \text{ V/m}$  and undergo FIDI at  $2.18 \times 10^6 \text{ V/m}$ , the latter is taken as  $E_c^0$ . The shape of droplets undergoing FIDI at  $E_c^0$  ( $\nabla$ ) resembles the shape of oscillating droplets through half a period as is noted by the similar values of  $\gamma(t)$  through 450  $\mu\text{s}$ . This shows that oscillation frequencies may be employed to predict FIDI timescales. Above  $E_c^0$  the elongation is accelerated, resulting in a decrease in the time needed to reach jetting and progeny formation.

Figure 7.6 also provides insight regarding the fitted oscillation frequency values shown in Figure 7.4. Although the fitted oscillation frequency values most closely match the trend of Brazier-Smith and coworkers,  $\nu^{\text{BS}}$ , that theory predicts the shape oscillation decreases to zero as the applied field reaches  $E_c^0$ . The similarity between the oscillating droplet and the aspect ratio of droplets undergoing FIDI at  $E_c^0$  in Figure 7.6 demonstrates that sub-critical oscillations decrease to a finite, non-zero value. The analytical model of Feng and Beard and the numerical model of Basaran and co-workers provide the closest theoretical match with our measured oscillation frequencies. In using equation (7.10) to predict the FIDI behavior of a droplet of known physical parameters, equation (7.8) currently provides the best approximation of the timescale for progeny drop formation at  $E_c^0$ .

#### 7.4.3. Case Three. Charged droplets above the critical field

Figure 7.7 and Figure 7.8 show asymmetrical stretching and jetting from charged 225  $\mu\text{m}$  methanol droplets. Figure 7.7A-E shows droplets carrying a charge 0.04  $q_R$  in a  $2.16 \times 10^6 \text{ V/m}$  field and 0.09  $q_R$  droplets in a  $2.14 \times 10^6 \text{ V/m}$  field in frames (F)-(J). In both cases, droplets are exposed to the minimum field required for jetting,  $E_c^q$ , for each respective  $q$ . Similarly, Figure 7.8A-H displays a sequence of 0.13  $q_R$  droplets at their critical field of  $2.09 \times 10^6 \text{ V/m}$ . The non-linear trend in decreasing critical fields agrees with finite-element calculations<sup>12</sup> and disagrees with the linear dependence on charge determined by Abbas and Latham.<sup>24</sup> Similarly, the time to initiate jetting decreases as

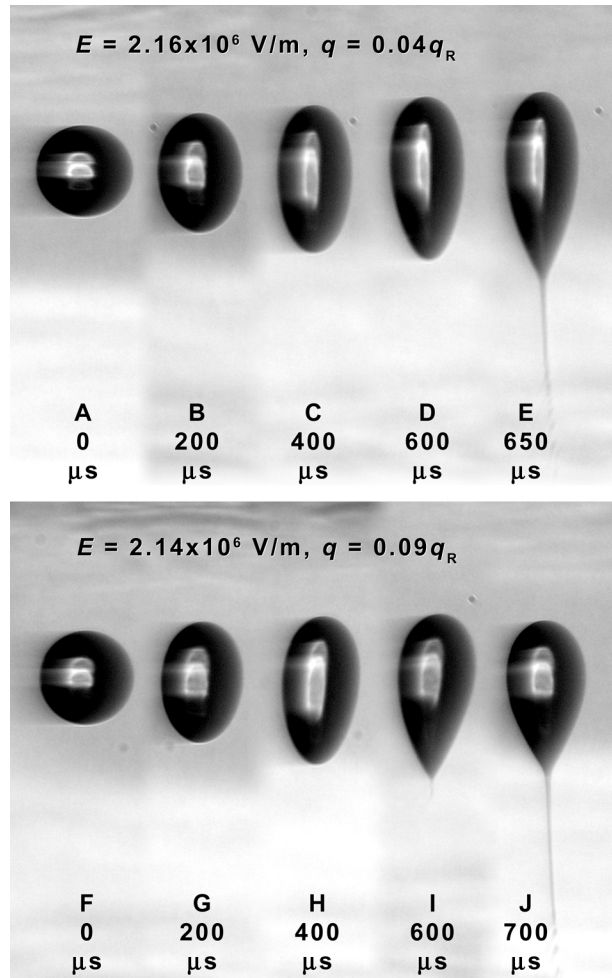


Figure 7.7. Sequences of  $225 \mu\text{m}$  methanol droplets with  $q = 0.04 q_R$  droplets undergoing asymmetrical distortions at  $E = 2.16 \times 10^6 \text{ V/m}$  and  $q = 0.09 q_R$  droplets at  $E = 2.14 \times 10^6 \text{ V/m}$ . In both cases, these fields represent the minimum for which FIDI is observed,  $E_c^q$ . For  $0.04 q_R$ , the  $650 \mu\text{s}$  time to begin jetting (E) is identical to the corresponding neutral droplet at  $E_c^0$  (Figure 5E) while  $0.09 q_R$  droplets exhibit a nascent jet at  $600 \mu\text{s}$  (I). The jets in (E) and (J) demonstrate capillary instability and the formation of  $\sim 10 \mu\text{m}$  progeny droplets.

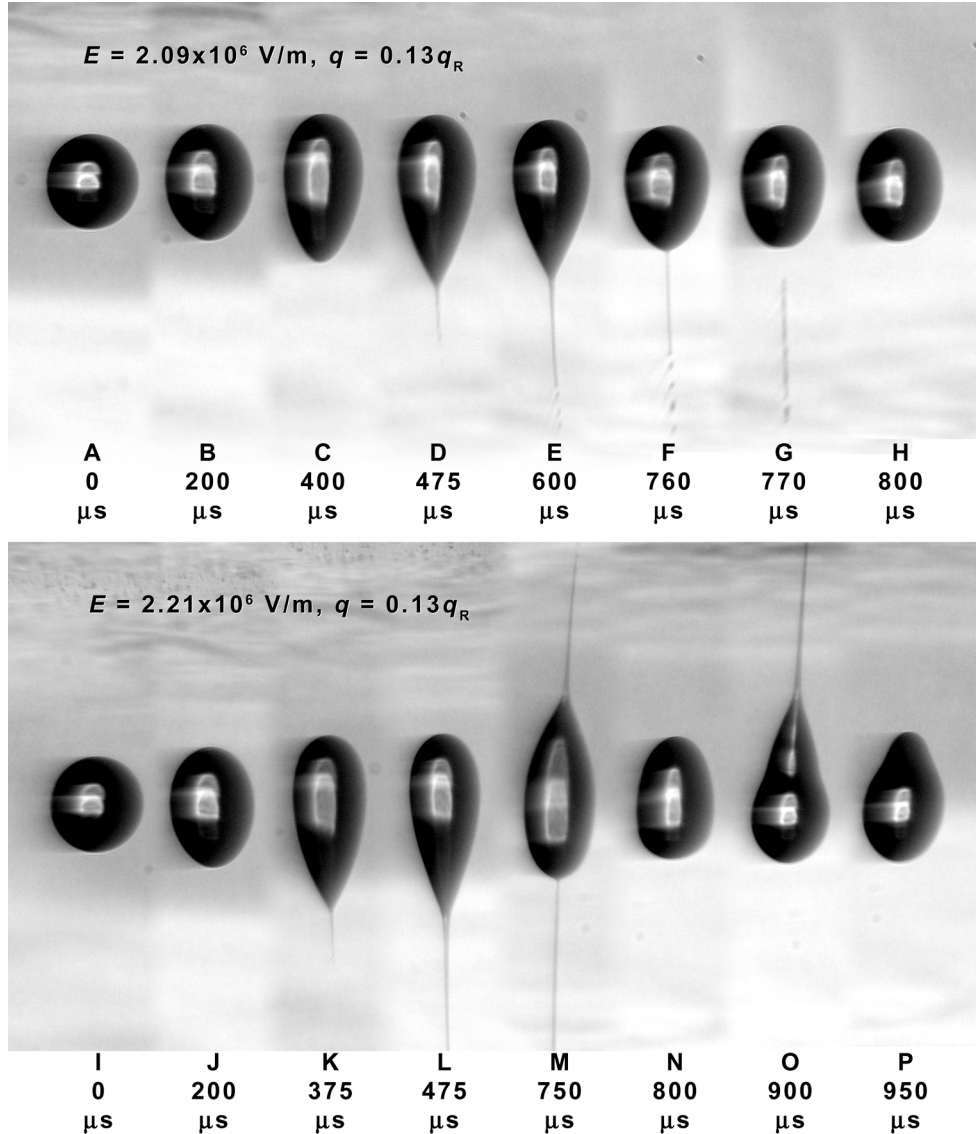


Figure 7.8. Sequences of 225  $\mu\text{m}$  methanol droplets with  $q = 0.13 q_R$  in a  $2.09 \times 10^6$  (A)-(H) and a  $2.21 \times 10^6$  V/m field (I)-(P). For these droplets  $E_c^q = 2.09 \times 10^6$  V/m. Extended observation at  $E_c^q$  demonstrates the entire FIDI process from distortions (A)-(C), jetting (D)-(G), and back to a spheroidal shape (H). Drops (E) through (G) distinctly show the formation of fine progeny. As the jetting concludes in (F)-(G), both the aspect ratio and the size of the Taylor cone decrease. The  $2.21 \times 10^6$  V/m field in (I)-(J) is greater than  $E_c^0$  for neutral droplets and results in sequential jetting of a positive jet from 375  $\mu\text{s}$  (K) through 750  $\mu\text{s}$  (M) where a short-lived negative jet appears. Following initial jetting, droplets develop non-conical distortions and emit an additional short-lived negative jet at 900  $\mu\text{s}$  (O). The non-conical shape and second negative jet are attributed to higher-order vibrations caused by the initial asymmetric flow within the droplet.

net charge increases. At  $0.04 q_R$ , jet formation occurs at  $650 \mu\text{s}$  as shown in Figure 7.7E which is the same timescale observed for neutral droplets at  $E_c^0$  (Figure 7.5E). As the charge increases, the timescale decreases to  $600 \mu\text{s}$  at  $0.09 q_R$  (Figure 7.7I) and  $475 \mu\text{s}$  at  $13\% q_R$  (Figure 7.8D).

Figure 7.8 includes photographs illustrating the behavior of droplets beyond the initial jetting process. Figure 7.8D shows a sharp Taylor cone emitting a progeny jet at  $475 \mu\text{s}$ . The initial stages of jetting correspond to the sharpest cones. By  $760 \mu\text{s}$  (Figure 7.8F), the cone has receded as the jet is emitted from a roughly spheroidal droplet. In frame (G), ten microseconds later, the progeny jet has separated from the completely spheroidal parent. In this case, the duration of the FIDI event is approximately  $285 \mu\text{s}$ .

At higher fields, charged droplets exhibit sequential jetting. Figure 7.8I-P illustrates the response of  $0.13 q_R$  charged droplets to a  $2.21 \times 10^6 \text{ V/m}$  electric field that is 6% higher than  $E_c^q$  and 2% greater than  $E_c^0$  for neutral droplets of the same size. Droplets distort asymmetrically and emit a *positive* jet from  $375 \mu\text{s}$  (Figure 7.8K) through  $750 \mu\text{s}$  (M). Unique to this case, droplets develop a second conical tip that emits a short-lived *negative* progeny jet at  $750 \mu\text{s}$  (M). After this sequential jetting, droplets relax into a spade-shaped configuration (frame N) before emitting an additional short-lived negative jet at  $900 \mu\text{s}$  (frame O) from a non-conical tip. We attribute the spade and non-conical shapes of the second negative jet in Figure 7.8N-P to higher-order,  $l > 2$ , mode vibrations within the droplet where  $l = 2$  is the fundamental mode.<sup>35,36</sup> Higher-order vibrations are most likely due to asymmetric flow within the droplet during the initial asymmetric elongation in frames (A)-(D) and the corresponding relaxation in (F)-(H).

#### 7.4.4. Progeny droplet and parent charge loss

Figure 7.7 and Figure 7.8 show progeny droplets separating from the charged droplet jet. Progeny droplets appear at the end of jets from both charged and neutral parents and form due to capillary instability and breakup of the jet. These progeny droplets are approximately 10  $\mu\text{m}$  across or roughly 5% of the diameter of the 225  $\mu\text{m}$  parent droplets. The present experiment is unable to quantify a decrease in size of the parent droplet after a FIDI event such as the sequence in Figure 7.8A-H, and therefore observations of mass loss are below the measurement limits of the optical train. If the upper limit of mass loss were bounded at 5%, then 600 progeny droplets, each 10  $\mu\text{m}$  in diameter, would result. The lower bound is the volume within a cylindrical jet at any instant. Jets extend 600  $\mu\text{m}$  to the electrodes, and a 10  $\mu\text{m}$  diameter cylinder of liquid methanol would form ninety 10  $\mu\text{m}$  progeny droplets.

Measurements of the current associated with the droplets stream provide information relating to the droplet charge. Droplets carrying a  $+0.03 q_R$  net charge produce a 4.5 nA current with  $E = 0$ . When the electric field is applied, the timing cycle relative to the droplet flow is such that only 5% of the droplets produced undergo FIDI at a sufficiently high field strength. The remainder of the droplets pass between the electrodes when they are both at high voltage and there is no field between them. The droplets undergoing FIDI lead to a decrease in the picoammeter current of 1.0 nA, indicating that an individual droplet experiences a 1.8 pC loss or  $0.13 q_R$  per FIDI event. Because the droplets initially carried a  $+0.03 q_R$  charge, the FIDI event leaves the droplets *oppositely charged*  $-0.10 q_R$ . This observation is consistent with the data in Figure 7.8I-P where following the initial jetting process, the droplets emit jets in the opposite direction.

#### 7.4.5. Droplet images in the literature

The images of symmetrical neutral droplet jetting in Figure 7.5 and asymmetrical charged droplet jetting in Figure 7.7 and Figure 7.8 can be related to previous photographs of droplet instabilities and jetting. Hager and co-workers imaged jetting from charged methanol droplets in the high electric field used to generate a corona discharge.<sup>37,38</sup> Droplets distorted asymmetrically and emitted a single jet of progeny directed away from the corona needle along the field lines. Reported figures were overlays of 3000 individual photographs indicating a highly reproducible jetting phenomenon. Gomez and Tang captured heptane droplets undergoing asymmetrical jetting in an electrospray plume.<sup>39</sup> The images of heptane droplets are single events not consistently oriented with the electric field within the electrospray plume. They attribute this to aerodynamic effects. In both the Hager and co-workers and the Gomez and Tang experiments, the droplets carried a net charge before jetting as a result of being ionized by the corona discharge or the electrospray process, respectively. Similarly, both were observed in high fields, specifically a corona discharge and an electrospray plume. While both sets of images are inferred to be the result of Rayleigh discharge events,<sup>8</sup> the asymmetrical nature contrasts with the symmetrical event observed by Duft and co-workers for charged ethylene glycol droplets suspended in an electrodynamic balance (EDB).<sup>16</sup> The droplets studied by Hager and co-workers most likely exhibit jetting induced by an electric field, corresponding to Case 3, rather than a pure Rayleigh discharge process. The situation is less clear with the Gomez and Tang experiments. In

the dense electrospray plume, the electric fields of nearby charged droplets may also affect the jetting process when droplets approach the Rayleigh limit.

#### **7.4.6. Implications for FIDI-mass spectrometry**

The neutral and charged droplet studies in Cases 2 and 3 suggest new methods of sampling in FIDI-MS. The minimum field necessary for neutral droplet FIDI is given by (7.2) and the timescale of the event is predicted by (7.10). Charged droplets develop instabilities and undergo FIDI sooner than their neutral counterparts, and increasing the applied electric field above the critical value also decreases the timescale. For example, the time needed to induce jetting and charged progeny formation from 225  $\mu\text{m}$  methanol droplets is reduced by almost half when the field is raised from  $E_c^0$  to 6% higher than  $E_c^q$  and the charge is increased from 0 to 0.13  $q_R$  (Figure 7.8). This may be applied to analyze the composition of a specific droplet out of a larger collection selectively charged in a manner similar to flow cytometry experiments, or a single charged droplet held in an EDB. Takeda and co-workers recently demonstrated that electric fields lift water droplets off of a superhydrophobic surface in a process that imparts a net charge to the droplet.<sup>40</sup> These droplets can subsequently be directed into a high-field region for FIDI-MS analysis. This technique may be applied to sample the composition of droplets from a microfluidic device or an LC column.

### **7.5. Conclusions**

A droplet stability diagram in Figure 7.9 summarizes the behavior of droplets as a function of charge and applied electric field. Neutral droplets (Figure 7.9A) experience

prolate shape oscillations in fields below a critical strength,  $E_c^0$ . Above  $E_c^0$  (Figure 7.9B), droplets form symmetric cone-jets of positive and negative progeny at a rate that may be predicted from the frequency of the sub-critical shape oscillations. Thus theoretical models of shape oscillations are important for studying new systems, as the timescale for the onset of jetting at  $E_c^0$  is approximately 75% the oscillation period slightly below  $E_c^0$ .

The critical limit for charged droplets,  $E_c^q$ , decreases as charge is increased. This non-linear limit is represented by the solid curve in Figure 7.9 and qualitatively follows the shape predicted both by numerical analysis and Taylor's spheroidal approximation.<sup>12</sup> Below  $E_c^q$ , tear-shaped oscillations are found in charged droplets (Figure 7.9C) while above  $E_c^q$  droplets emit a single charged jet of progeny droplets (Figure 7.9D). At fields above  $E_c^0$  a new behavior is observed in which charged droplets sequentially emit a jet of the same polarity as the net charge followed by a jet of reverse polarity from the opposing side (Figure 7.9E). The critical limit for sequential jetting is noted by the dashed curve whose specific shape remains unexplored over a wide range of  $q$ - $E$  space.

Increasing the electric field decreases the time to form jets from both neutral and charged droplets, and the combination of net charge and higher-than-critical electric fields has a compound effect in accelerating progeny formation. Therefore the period of neutral droplet shape oscillations represents a maximum timescale for the onset of FIDI. Understanding the FIDI characteristics for a droplet of given size and charge in a specific applied field, one may apply rapidly switched fields to directly mass analyze the components of a specific droplet or a single droplet held in an electrodynamic balance.

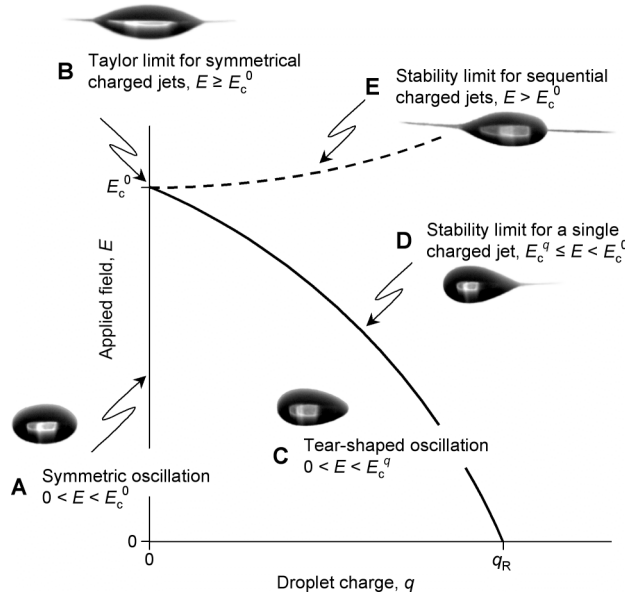


Figure 7.9. Summary of droplet stability as a function of net charge and applied electric field. Uncharged droplets below the critical field  $E_c^0$  (A) undergo symmetric shape oscillations. Above  $E_c^0$ , uncharged droplets in fields above  $E_c^0$  symmetrically elongate and simultaneously emit positive and negative progeny jets (B). The critical field for progeny formation from charged droplets decreases with increasing charge, represented by  $E_c^q$  (solid curve). Below  $E_c^q$ , charged droplets oscillate with asymmetric, tear shapes (C). Above  $E_c^q$ , droplets emit a single jet of charged progeny (D). At fields greater than  $E_c^0$ , a second critical field exists above which charged droplets emit sequential jets (E). The curve of this stability limit is unknown and represented with a dashed line.

## 7.6. Acknowledgements

The authors thank Dr. Richard Flagan for his discussions and Dr. Thomas Leisner for the LabView-based droplet analysis software. This material is based on work supported by the National Science Foundation under grant No. CHE-0416381 and a grant from the Beckman Institute at Caltech.

## 7.7. References

- (1) Grimm, R. L.; Beauchamp, J. L. *J. Phys. Chem. B* **2003**, *107*, 14161.
- (2) Wilson, C. T. R. *Phil. Trans. A* **1921**, *221*, 104.
- (3) Wilson, C. T. R.; Taylor, G. I. *Proc. Cambridge Philos. Soc.* **1925**, *22*, 728.
- (4) Nolan, J. J. *Proc. R. Ir. Acad. Sect. A* **1926**, *37*, 28.
- (5) Bailey, A. G. *Electrostatic spraying of liquids*; Wiley: New York, 1988.
- (6) Fenn, J. B.; Mann, M.; Meng, C. K.; Wong, S. F.; Whitehouse, C. M. *Science* **1989**, *246*, 64.
- (7) Yamashita, M.; Fenn, J. B. *J. Phys. Chem.* **1984**, *88*, 4451.
- (8) *Electrospray Ionization Mass Spectrometry*; Cole, R. B., Ed.; John Wiley and Sons: New York, 1997.
- (9) Kebarle, P. *J. Mass Spectrom.* **2000**, *35*, 804.
- (10) Grimm, R. L.; Beauchamp, J. L. *Anal. Chem.* **2002**, *74*, 6291.
- (11) Smith, J. N.; Flagan, R. C.; Beauchamp, J. L. *J. Phys. Chem. A* **2002**, *106*, 9957.
- (12) Basaran, O. A.; Scriven, L. E. *Phys. Fluids A* **1989**, *1*, 799.
- (13) Basaran, O. A.; Patzek, T. W.; Benner, R. E.; Scriven, L. E. *Ind. Eng. Chem. Res.* **1995**, *34*, 3454.
- (14) Rayleigh, L. *Philos. Mag.* **1882**, *14*, 184.
- (15) Davis, E. J.; Bridges, M. A. *J. Aerosol Sci.* **1994**, *25*, 1179.
- (16) Duft, D.; Atchtzehn, T.; Muller, R.; Huber, B. A.; Leisner, T. *Nature* **2003**, *421*, 6919.
- (17) Zeleny, J. *Phys. Rev.* **1917**, *10*, 1.
- (18) Macky, W. A. *Proc. Roy. Soc. A* **1931**, *133*, 565.
- (19) O'Konski, C. T.; Thacher, H. C. *J. Phys. Chem.* **1953**, *57*, 955.
- (20) Taylor, G. *Proc. R. Soc. London, Ser. A* **1964**, *280*, 383.

- (21) Inculet, I. I.; Kromann, R. *IEEE Trans. Ind. Appl.* **1989**, *25*, 945.
- (22) Saville, D. A. *Annu. Rev. Fluid Mech.* **1997**, *29*, 27.
- (23) Abbas, M. A.; Latham, J. *J. Fluid Mech.* **1967**, *30*, 663.
- (24) Abbas, M. A.; Latham, J. *Q. J. R. Met. Soc.* **1969**, *95*, 63.
- (25) Vizika, O.; Saville, D. A. *J. Fluid Mech.* **1992**, *239*, 1.
- (26) Ha, J. W.; Yang, S. M. *J. Fluid Mech.* **2002**, *405*, 131.
- (27) Eow, J. S.; Ghadiri, M. *Chem. Eng. Process.* **2003**, *42*, 259.
- (28) Chen, B. T.; John, W. Instrument Calibration. In *Aerosol Measurement: Principles, Techniques, and Applications*; Baron, P. A., Willeke, K., Eds.; Wiley-Interscience: New York, 2001; pp 627.
- (29) Dahl, D. A. *SIMION 3D*; Idaho Natl. Eng. and Environ. Lab.: Idaho Falls, Idaho, 2000.
- (30) Baker, R. J.; Johnson, B. P. *Rev. Sci. Instrum.* **1992**, *63*, 5799.
- (31) Continetti, D. M.; Cyr, D. R.; Neumark, D. M. *Rev. Sci. Instrum.* **1992**, *63*, 1840.
- (32) Leisner, T. *Spindle analysis program*; Technische Universität Ilmenau: Ilmenau, Germany, 2004.
- (33) Feng, J. Q.; Beard, K. V. *Proc. R. Soc. London, Ser. A* **1990**, *430*, 133.
- (34) Brazier-Smith, P. R.; Brook, M.; Latham, J.; Saunders, C. P.; Smith, M. H. *Proc. R. Soc. London, Ser. A* **1971**, *322*, 523.
- (35) Becker, E.; Hiller, W. J.; Kowalewski, T. A. *J. Fluid Mech.* **1991**, *231*, 189.
- (36) Basaran, O. A.; Scriven, L. E. *Phys. Fluids A* **1989**, *1*, 795.
- (37) Hager, D. B.; Dovichi, N. J.; Klassen, J.; Kebarle, P. *Anal. Chem.* **1994**, *66*, 3944.
- (38) Hager, D. B.; Dovichi, N. J. *Anal. Chem.* **1994**, *66*, 1593.
- (39) Gomez, A.; Tang, K. *Phys. Fluids* **1994**, *6*, 404.
- (40) Takeda, K.; Nakajima, A.; Hashimoto, K.; Watanabe, T. *Surf. Sci.* **2002**, *519*, L589.

